

SPITZER OBSERVATIONS OF LOW LUMINOSITY ISOLATED AND LOW SURFACE BRIGHTNESS GALAXIES

J. L. HINZ, M. J. RIEKE, G. H. RIEKE, C. N. A. WILLMER, K. MISSELT, C. W. ENGELBRACHT, M. BLAYLOCK
Steward Observatory, University of Arizona, 933 N. Cherry Ave., Tucson, AZ 85721
email: jhinz, mrieke, grieke, cnaw, kmissett, cengelbracht, blaylock@as.arizona.edu

T. E. PICKERING

MMT Observatory, Smithsonian Institution and University of Arizona, Tucson, AZ 85721
email: tim@mmto.org

Draft version October 26, 2018

ABSTRACT

We examine the infrared properties of five low surface brightness galaxies (LSBGs) and compare them with related but higher surface brightness galaxies, using *Spitzer Space Telescope* images and spectra. All the LSBGs are detected in the 3.6 and 4.5 μm bands, representing the stellar population. All but one are detected at 5.8 and 8.0 μm , revealing emission from hot dust and aromatic molecules, though many are faint or point-like at these wavelengths. Detections of LSBGs at the far-infrared wavelengths, 24, 70, and 160 μm , are varied in morphology and brightness, with only two detections at 160 μm , resulting in highly varied spectral energy distributions. Consistent with previous expectations for these galaxies, we find that detectable dust components exist for only some LSBGs, with the strength of dust emission dependent on the existence of bright star forming regions. However, the far-infrared emission may be relatively weak compared with normal star-forming galaxies.

Subject headings: galaxies: evolution - galaxies: photometry

1. INTRODUCTION

Low surface brightness galaxies (LSBGs), defined as those with B -band central surface brightnesses, $\mu_{0,B}$, fainter than 23.0 mag arcsec⁻², appear to have followed a very different evolutionary history from high surface brightness galaxies (e.g., McGaugh 1992; Knezek 1993). Their stellar populations, stellar masses, current star formation rates, and other properties appear to differ significantly from their high surface brightness counterparts, and little is known about their corresponding dust properties. A better understanding of these differences is needed to understand how they evolved to their present state.

It has been generally assumed, even though a population of red LSBGs has been discovered (O’Neil et al. 1997a), that they contain little dust, and dust reddening has not been considered an important effect (e.g., Bothun et al. 1997; Bell et al. 2000). LSBGs have low star formation rates, with suspected modest bursts in the range 10⁻³-10⁻² M_⊙ yr⁻¹ (e.g., Vallenari et al. 2005) and low metallicities, with almost all LSBGs at or less than about one-third solar (McGaugh 1994; Ronnback & Bergvall 1995). Their low metallicities imply that the dust to gas ratios should be systematically lower than in their high surface brightness galaxy counterparts, and the fact that the *Infrared Astronomical Satellite* (*IRAS*; Neugebauer et al. 1984) and the *Infrared Space Observatory* (*ISO*; Kessler et al. 1996) were only able to detect two of these galaxies seems to indicate that dust is much less important in LSBGs. Furthermore, any data acquired with these observatories would not have been adequate to characterize dust temperatures or spatial distributions.

That dust plays a relatively minor role in the evolution of LSBGs is further reinforced by observations of highly transparent galaxies that appear to have multi-

ple distant galaxies seen through their disks (O’Neil et al. 1997b; P. Knezek, private communication). This has been confirmed by a more detailed analysis of the dust opacity of LSBG disks in comparison to those of high surface brightness galaxies, where LSBGs appear effectively transparent (Holwerda et al. 2005).

Additionally, Pickering & van der Hulst (1999) attempted to detect dust in LSBGs using submillimeter observations from the JCMT with SCUBA. Ten galaxies were observed, two of which were detected at 850 μm with only one detected at 450 μm . They combined their submillimeter data with existing *IRAS* data, finding dust temperatures in the range 15-20 K. None of their very LSB ($\mu_B \leq 23.5$) galaxies were detected, and they concluded that the lack of detection in the lowest surface brightness galaxies was consistent with previous lines of evidence that only modest amounts of dust could exist.

Spitzer opens the opportunity to study any dust that may exist at low levels in LSBGs. The increased sensitivity relative to previous observations gives a higher likelihood of the detection of diffuse dust emission that echoes the LSBGs’ diffuse optical appearance. In addition, the resolution of the *Spitzer* imaging instruments allows for analysis of dust temperature, mass, and spatial distribution in LSBGs not possible before, making it feasible to address crucial issues regarding chemical evolution and dust production. We present here the infrared properties of a small sample of LSBGs with the full suite of *Spitzer* instruments.

2. OBSERVATIONS

All *Spitzer* observations presented here are part of the Dust in Low Surface Brightness Galaxies Guaranteed Time Observation Program (P.I.D. 62) whose Principal Investigator is M. J. Rieke.

2.1. Sample

The galaxies in this sample were selected to be some of the brightest and closest known LSBGs, many taken from the work of Pickering (1998). Two galaxies are high surface brightness, low metallicity isolated late-type spirals that are included for the purpose of comparison with the LSBGs. Table 1 summarizes general information for each galaxy, with the LSBGs and high surface brightness galaxies separated by a line. The objects were chosen such that the infrared background cirrus was low, improving the chances of detection of the faintest emission associated with each galaxy, and with sufficiently large angular diameters for resolution with the *Spitzer* instruments. Here we briefly outline their main properties and unique characteristics.

2.1.1. Low Surface Brightness Galaxies

Malin 1 is one of the best known LSBGs (Bothun et al. 1987; see Barth 2007 for a more recent view) and the largest gas-rich galaxy found to date. Its optical disk is six times bigger than that of the Milky Way. Its spectrum is dominated by its old, metal-rich stellar population, with a smaller contribution from hot, young stars (Impey & Bothun 1989). This LSBG is the most distant object in our sample.

UGC 5675: This Magellanic dwarf spiral (e.g., Schneider et al. 1990; McGaugh et al. 1995) has a very low surface brightness disk (Schombert & Bothun 1988) and has the faintest M_B of our sample. It does not have any regions of distinct star formation or an extended H I envelope (van Zee et al. 1995).

UGC 6151 is another Magellanic spiral with a small core of optical emission surrounded by faint diffuse emission with little structure. McGaugh et al. (1995) note that the galaxy contains “quite a few faint H II regions”.

UGC 6614 has a star-forming distinctive ring and has a particularly extended disk that can be traced to at least $130''$ (van der Hulst et al. 1993). It is the most metal-rich LSBG known and is considered to be a “cousin” to Malin 1 due to their similar properties. The H I data show that there is a central depression in the gas distribution, which has led to discordant flux measurements in the literature (Bothun et al. 1985; Giovanelli & Haynes 1989; Pickering et al. 1997; Matthews et al. 2001), although the most recent of these works agree.

UGC 9024: This galaxy has a very low surface brightness disk coupled with a normal bulge. It has been suggested that the large disk plus bulge indicates that it is a transition object between average sized LSBGs with no bulge and giant Malin 1 type galaxies (McGaugh et al. 1995).

2.1.2. High Surface Brightness Galaxies

UGC 6879: This object, while in the Impey et al. (1996) catalogue of low surface brightness galaxies, does not qualify as an LSBG, due to its bright central surface brightness. (It is possible that it was either a candidate LSBG, later observed and found to be too bright, or that it qualified as a type of LSB disk using a “diffuseness” index involving the disk scale length; see Sprayberry et al. 1995 for details). This galaxy is one of the few in the program to have been detected by *IRAS*, with photometry measurements at 60 and $100\ \mu\text{m}$ and upper limits at 12

and $25\ \mu\text{m}$. It also has a detection at $850\ \mu\text{m}$ by SCUBA (Pickering & van der Hulst 1999), making it an excellent candidate for further study in the mid- and far-IR at the higher sensitivity and resolution of *Spitzer*.

UGC 10445 is a nearby starbursting dwarf spiral. The *Spitzer* images of this object have been examined in detail in Hinz et al. (2006). It also has available *IRAS* and *ISO* measurements.

2.2. Data

Each galaxy was observed with the Infrared Array Camera (IRAC; Fazio et al. 2004) at all four wavelengths (3.6 , 4.5 , 5.8 , and $8.0\ \mu\text{m}$), in one $5' \times 5'$ field with a frame time of 30 s and with a dither of five positions Gaussian, for a total integration time of 150 s per object per wavelength. IRAC data were reduced at the *Spitzer* Science Center (SSC) with the S14.0.0 pipeline. The IRAC spatial resolution is $\sim 2''$ in all bands.

The Multiband Imaging Photometer for *Spitzer* (MIPS; Rieke et al. 2004) data for the sample were observed in photometry mode at 24, 70, and $160\ \mu\text{m}$. The integration times on all galaxies were 690 s at $24\ \mu\text{m}$, 252 s at $70\ \mu\text{m}$, and 42 s at $160\ \mu\text{m}$. The MIPS data were reduced using the Data Analysis Tool version 3.00 (DAT; Gordon et al. 2005), the same techniques that are used to calibrate the instrument itself. Two independent reductions were carried out to test for systematic errors on these faint sources; the results agreed closely for both reductions. The MIPS spatial resolutions are $6''$, $18''$, and $40''$ at 24, 70, and $160\ \mu\text{m}$, respectively. Dates for the IRAC and MIPS observations are given in Table 1. The MIPS $24\ \mu\text{m}$ observations for UGC 5675 appear to be corrupted. The observations performed by *Spitzer* just prior to this object were deep, high-redshift observations and unlikely to introduce saturated objects that might have effected our data set. However, the southwestern corner of almost all the $24\ \mu\text{m}$ data collection events have highly saturated pixels marked as NaN. Further processing and mosaicing of the image was impossible, and no information could be recovered.

Infrared Spectrograph (IRS; Houck et al. 2004) staring-mode observations were scheduled for only three of the targets in this program: Malin 1, UGC 6879, and UGC 10445. Galaxies were observed in the low resolution 5.2 - $8.7\ \mu\text{m}$ (SL2) and 7.4 - $14.5\ \mu\text{m}$ (SL1) modes and in the low resolution 14.0 - $21.3\ \mu\text{m}$ (LL2) and 19.5 - $38\ \mu\text{m}$ channels (LL1). Details of the observations, including dates, integration times and slit position angles, are given in Table 2. The faint, diffuse, and complex nature of these sources makes such observations difficult. *Spitzer*’s onboard peak-up algorithm centroided on a source considered far from the intended target position for UGC 10445 and centroided on a bad pixel rather than Malin 1. Data were reduced with version S13.2.0 of the SSC data pipeline, with extractions using the pipeline developed by the Formation and Evolution of Planetary Systems (FEPS) Legacy team (Hines et al. 2006).

Additional data are available for UGC 6879. These include the far and near-ultraviolet (1350 - $1750\ \text{\AA}$, $\lambda_{eff} = 1516\ \text{\AA}$, and 1750 - $2750\ \text{\AA}$, $\lambda_{eff} = 2267\ \text{\AA}$, respectively) images from *Galaxy Evolution Explorer* (*GALEX*; Martin et al. 2005) made available through the NASA Extragalactic Database (NED).

3. ANALYSIS

3.1. Morphology

Figure 1 shows an image of each galaxy in the sample at all the *Spitzer* wavelengths, with the exception of UGC 10445, which was presented by Hinz et al. (2006).

IRAC detects all galaxies in the sample at 3.6 and 4.5 μm and all except for UGC 5675 at 5.8 and 8.0 μm . In general, the LSBGs are easily detected at the two shorter wavelength bands, representing the old stellar population, and difficult to image at 5.8 and 8.0 μm , with many having only point-like detections at the longer wavelengths.

The MIPS observations of the LSBGs are varied. There are clear detections of all LSBGs at 24 μm (with the exception of the corrupted data of UGC 5675, as explained above), three detections at 70 μm , and two at 160 μm . Of these detections, two have extended emission at 24 μm while two have point-like morphologies. At 70 μm , two are extended, with one point-like, and at 160 μm two are extended, with no point-like detections. A summary of this rough classification is given in Table 3, with LSBGs listed above the solid line and HSBGs listed below the solid line.

The difficulty of detecting emission at the longer wavelengths for the LSBGs is not simply a result of the decreased resolution. Figure 2 shows the three MIPS images of UGC 6614, with both the 24 and 70 μm images convolved with a kernel that transforms them to the resolution of the 160 μm data. The kernel was created using a Fourier technique on the MIPS PSFs generated by STinyTim (Gordon et al. in preparation). The galaxy seems to be more extended at 70 μm than at 24 μm , consistent with the star forming ring becoming more prominent as shown in Figure 1. The signal to noise is too low at 160 μm to confirm this trend, but the image does show that the peak remains on the galaxy center, as defined at 24 and 70 μm . The changing brightness and morphology of the galaxy does not seem to be related to the resolution differences.

3.2. Photometry

Aperture photometry was conducted on all *Spitzer* images. Additional image processing in the form of background subtraction was first completed by subtracting a constant value from each image. The value of this constant was determined by masking stars in the foreground, then taking an average of all pixel values outside the aperture used for the galaxy photometry. For galaxies where the foreground contamination was particularly high, we used a large region surrounding the galaxy to determine a background value that included a sampling of foreground stars. Table 3 shows the MIPS flux density values and their associated errors, along with the radii of apertures used. Table 4 shows the corresponding IRAC photometry values. Galaxies that are undetected at the various wavelengths have 3σ upper limits listed in Tables 3 and 4. Upper limits were calculated from the images themselves, using the mean value of the sky counts and adding three times the value of the standard deviation of the sky counts.

The photometric uncertainties are estimated to be 10% at 3.6 and 4.5 μm and 15% at 5.8 and 8.0 μm . These values include a 3% absolute calibration uncertainty (Reach

et al. 2005), a contribution for scattered light in an extended source (W. Reach, private communication), and an uncertainty due to the sensitivity of the measurements to the background subtraction. The contribution of the scattered light is higher at 5.8 and 8.0 μm . We do not perform aperture corrections on the IRAC photometry, which in certain limiting cases can be up to 25-30% for the 5.8 and 8.0 μm bands. In our case, it is difficult to determine this correction for the mixture of point and extended sources seen in the IRAC images. We mainly use the 8.0 μm images to establish the presence of aromatic feature emission in our galaxies, so uncertainties of this magnitude have no effect on our conclusions. The MIPS flux calibration uncertainties are 4% at 24 μm , 7% at 70 μm , and 12% at 160 μm (Engelbracht et al. 2007; Gordon et al. 2007; Stansberry et al. 2007). Photometric uncertainties bring these values to total errors of 10% at 24 μm , 20% at 70 μm , and 20% at 160 μm .

3.3. Dust Modeling for UGC 6879

UGC 6879, with its bright detections at all IR wavelengths, can be analyzed in detail based on the mid-infrared and submillimeter photometry. Figure 3 shows the spectral energy distribution (SED) for this galaxy, including *GALEX*, 2MASS, IRAC, *IRAS*, *Spitzer*, and SCUBA data points. The emission by dust at the longer wavelengths can be modeled by an equation of the form

$$F_{dust}(\lambda) = \sum C_i \kappa_i(\lambda) B_\lambda(T_{D,i}) \quad (1)$$

where $C_i = M_{dust,i}/D^2$ ($D \sim 32$ Mpc), κ_i is the mass absorption coefficient, B_λ is the Planck function, $M_{dust,i}$ is the dust mass, and the sum extends over the number of dust components. We adopt a two-component dust model consisting of warm and cool silicate grains ($a \sim 0.1$ μm). Further details regarding model assumptions and the fitting process can be found in Hinz et al. (2006). The data set is best fitted by a model consisting of a warm silicate component at $T = 51.51^{+1.41}_{-1.28}$ K and a cool silicate component at $14.94^{+0.53}_{-0.49}$ K, shown in Figure 3, where the quoted error bars are 1σ . We estimate the dust masses of UGC 6879 to be $8753^{+2469}_{-2017} M_\odot$ for the warm component and $3.50^{+0.63}_{-0.54} \times 10^7 M_\odot$ for the cool dust, where the quoted error bars are again 1σ . As shown in Hinz et al. (2006), choosing carbonaceous grains in place of silicate grains only modestly affects these values.

3.4. Spectroscopy

Figure 4 shows the full IRS spectra for UGC 6879, Malin 1, UGC 10445. We identify emission lines clearly detected in UGC 6879 and UGC 10445: [S IV], [Ne II], and [S III] (see, e.g., Smith et al. 2004). Additionally, we see the broad emission features usually attributed to polycyclic aromatic hydrocarbons (PAHs). The data show the four main aromatic bands at 6.2, 7.7, 8.6, and 11.3 μm . The aromatic feature at 12.7 μm is likely to be contaminated by the [Ne II] 12.8 μm line.

There are no spectral features detected in the Malin 1 spectrum. Despite the fact that *Spitzer* was not aligned on the coordinates given as the central nucleus of the galaxy, the large extent of Malin 1 ensures that IRS took data on some portion of the disk, and the exposure time

is long. Also, our photometry (Tables 3 and 4) shows the mid-IR excess to be very weak. It is likely that no aromatic features in Malin 1 are detectable with IRS in reasonable exposure times.

The spectra for UGC 6879 and UGC 10445 were fitted with the publicly available IDL tool PAHFIT, which was developed to decompose IRS spectra of PAH emission sources, with a special emphasis on the careful recovery of ambiguous silicate absorption, and weak, blended dust emission features (Smith et al. 2006).¹ The spectra were first prepared for PAHFIT by eliminating points with negative flux or with low ratios (≤ 2) of signal-to-noise. Table 5 shows the fluxes or equivalent widths (EW) for the various features as given by PAHFIT. The $7.7 \mu\text{m}$ complex is a sum of the 7.4 , 7.6 and $7.9 \mu\text{m}$ features. PAHFIT does not calculate uncertainties on equivalent widths because it is difficult to compute uncertainties on the continuum of the spectrum. The errors given in Table 5 assume that the fractional errors on the equivalent widths are the same as on the integrated features, and thus are lower limits.

4. DISCUSSION

4.1. Comparison of UGC 6879 and UGC 10445

The temperature of the cool dust, $T \sim 15 \text{ K}$, found for UGC 6879, a high surface brightness spiral, coincides with that found for the starbursting dwarf galaxy UGC 10445 (Hinz et al. 2006) using similar data and modeling techniques. It is also in agreement with the submillimeter temperature estimates of such dust in LSBGs by Pickering & van der Hulst (1999) and with infrared and submillimeter estimates of the temperatures of other low metallicity environments such as dwarf galaxies (Popescu et al. 2002; Lisenfeld et al. 2002; Bottnner et al. 2003). Additionally, observations of normalized high surface brightness galaxies, including the Milky Way (Reach et al. 1995; Lagache et al. 1998), show that cool dust components exist, and it is becoming apparent that such a cool component is fairly ubiquitous across galaxy types (see review by Tuffs & Popescu 2005).

The total calculated dust mass of UGC 6879 of $\sim 3.5 \times 10^7 M_{\odot}$ falls within the range found for normal high surface brightness spiral galaxies of $10^6 - 10^8 M_{\odot}$ (e.g., Sodroski et al. 1997; Bendo et al. 2003) and is a factor of ten higher than the mass values for UGC 10445 (Hinz et al. 2006). The cool dust mass value for UGC 10445 is considered a lower limit due to the fact that MIPS data are insensitive to dust colder than $T=15\text{-}20 \text{ K}$. The SCUBA $850 \mu\text{m}$ detection of UGC 6879 allows us to better estimate the turnover of the SED. The better constrained fits puts somewhat tighter constraints on the dust mass.

The H I gas mass to dust mass ratio found for UGC 10445 was ~ 500 (Hinz et al. 2006). This was found to be inconsistent with the mean value of the ratio for normal spiral galaxies (71 ± 49 ; Stevens et al. 2005), although the uncertainty in the dust mass value was large. The total H I mass for UGC 6879 is $1.10 \times 10^9 M_{\odot}$ (Sauty et al. 2003), giving a H I gas mass to dust mass ratio of 31_{-5}^{+6} . This value is consistent with the Stevens et al. (2005) mean value.

4.2. Comparison Between Low and High Surface Brightness Galaxies

Popescu et al. (2002) propose that cool dust in galaxies is heated by the diffuse non-ionizing ultraviolet radiation produced by young stars, with a small contribution from the optical radiation produced by old stars. This appears to be borne out for the high surface brightness galaxies, UGC 6879 and UGC 10445, where the *GALEX* and $24 \mu\text{m}$ images pinpoint the active star formation sites, and the corresponding $160 \mu\text{m}$ emission traces the detectable cool dust. Figure 5 shows the central *B*-band surface brightnesses for the sample versus the ratio of $24 \mu\text{m}$ to $160 \mu\text{m}$ flux density. The lower the central optical surface brightness for each object, the lower the this ratio appears to be. This implies that there are not large amounts of dust extinction; no highly obscured star formation is uncovered at $24 \mu\text{m}$, and those galaxies with the lowest surface brightnesses, i.e., without bright star-forming regions, are not detected at $160 \mu\text{m}$.

The appearance of broad aromatic emission spectral features in the isolated star-bursting galaxies confirms the presence of dust grains indicated by the IRAC, MIPS, *IRAS* and SCUBA images and photometry and our dust modeling. Aromatic emission is believed to originate mostly from photodissociation envelopes at the edges of star-forming regions that are bathed in ultraviolet photons, with some suggestion that B stars no longer associated with H II regions can also contribute to the heating (Spoon 2003; Calzetti et al. 2005). In the cases of UGC 6879 and UGC 10445, the high surface brightness galaxies for which we have IRS spectra, we clearly see star formation regions indicated by bright clumpy regions in the $24 \mu\text{m}$ images and the corresponding $8 \mu\text{m}$ emission that presumably accounts for the aromatic features.

In contrast, we see that the LSBG Malin 1 does not have dust emission at far-IR wavelengths, nor aromatic emission, which is not surprising, given the Popescu et al. (2002) model and explanation. Malin 1 exhibits no active star-forming regions detectable at any of the wavelengths that indicate such activity. Without those regions, UV photons cannot heat any existing dust to emit at long wavelengths, nor can the envelopes believed to be the site of aromatics exist. That is not to say that dust cannot exist in such an object, but simply that any such dust will not be heated and will not be detectable in far-IR images. This appears to be consistent with results for irregular dwarf galaxies, where aromatic emission is found only in the brightest H II regions or where there is widespread, intense star formation (Hunter et al. 2006). Braine et al. (2000) calculated an average star formation rate over a lifetime of 10^{10} yr for Malin 1 of $5 M_{\odot} \text{ yr}^{-1}$ based on its *V*-band luminosity. From this value they used Scoville & Young (1983) to derive a far-IR luminosity and translated this to an expected flux density of $\sim 100 \text{ mJy}$ at the *IRAS* $100 \mu\text{m}$ band. This was below the detection limit of *IRAS* and indeed was not detected. The longer integration times with MIPS now place that one-sigma upper limit at $160 \mu\text{m}$ of $\sim 10 \text{ mJy}$, with Malin 1 still invisible. One explanation for this low IR luminosity is that the current star formation rate is far below the average over the life of the galaxy.

Additionally, simply scaling the two-component dust model for high surface brightness galaxy UGC 6879 down

¹ Available at <http://turtle.as.arizona.edu/jdsmith/pahfit.php>.

to the $24\ \mu\text{m}$ flux density values for the LSBGs does not appear to fit their SEDs. A scaled model that fits, for instance, a $24\ \mu\text{m}$ flux density of $0.018\ \text{Jy}$, would predict a $70\ \mu\text{m}$ flux density of $\sim 0.4\ \text{Jy}$ and a $160\ \mu\text{m}$ flux density of $\sim 1.5\ \text{Jy}$. Comparing with the measurements of UGC 6614 shows 70 and $160\ \mu\text{m}$ outputs only $\sim 25\%$ of these predictions. The $160\ \mu\text{m}$ output of UGC 6151 also appears to be somewhat below the expected value. Therefore, it appears that the emission at the longer wavelengths for at least some LSBGs is fundamentally different from that of high surface brightness galaxies and that they are not simply low-luminosity versions of normal galaxies. Either LSBGs do not produce or maintain dust in the same quantities as other galaxies, or the dust is much colder and, therefore, undetectable in the far-IR.

Comparisons of the *Spitzer* data for different LSBGs may also reveal differences in evolutionary history. Figure 6 shows the IR SEDs of all the galaxies in the sample. While the two high surface brightness galaxies have similar SEDs from 3.6 to $160\ \mu\text{m}$, the LSBGs show a variety of steepnesses between wavelengths. Some have steepnesses from 24 to $160\ \mu\text{m}$ that are similar to the high surface brightness galaxies, while others are shallower (UGC 6614), and some appear to turn over after $70\ \mu\text{m}$ (UGC 9024). For instance, UGC 6151 and UGC 6614 have very similar far-IR flux densities, yet UGC 6614 is much brighter in red giant light, as represented by the $3.6\ \mu\text{m}$ flux density, compared with UGC 6151. This may imply that UGC 6614 formed stars at a much greater rate in the past, accumulating an old stellar population, while UGC 6151 may have formed stars at a more constant rate over its lifetime. The relatively high metallicity of UGC 6614 supports the hypothesis that its star formation was more vigorous in the past.

4.3. Metallicities and IR Properties of LSBGs

LSBGs are generally metal-poor, consistent with the well-known luminosity-metallicity ($L - Z$) relation for other galaxies (e.g., de Naray et al. 2004). In Figure 7 we show the metallicities of the entire HSBG plus LSBG sample versus the absolute magnitude at $24\ \mu\text{m}$. Absolute magnitudes are calculated using the MIPS $24\ \mu\text{m}$ magnitude zero point of 7.17 ± 0.0815 calculated by Engelbracht et al. (2007). Average metallicities are taken from a variety of sources in the literature (de Naray et al. 2004; McGaugh 1994). Others are calculated using the Sloan Digital Sky Survey - Sky Server.² Equivalent widths of optical emission lines such as [N II] and [O III] are available online, and we use those values in conjunction with the rough metallicity formulations of Wegner et al. (2003) and Salzer et al. (2005) to obtain metallicities. Metallicities are notoriously difficult to determine for LSBGs, and the variety of sources used to obtain them for this sample may inflate errors. However, Figure 7 shows a weak correlation in the expected direction that higher metallicity galaxies have brighter absolute magnitudes at $24\ \mu\text{m}$.

To probe the physical properties of galaxies that may contribute to the lack of aromatic emission features, we calculate R_1 , a comparison of the contribution of $8\ \mu\text{m}$ flux with the shorter IRAC wavelengths defined as

$(F_\nu(4.5\ \mu\text{m}) - \alpha F_\nu(3.6\ \mu\text{m}))/F_\nu(8\ \mu\text{m})$, and R_2 , which is the ratio of the 8 and $24\ \mu\text{m}$ flux densities, for all galaxies that are detected at those wavelengths (see Engelbracht et al. 2005 and their Figures 1 and 2). We show R_1 versus R_2 and R_2 versus the metallicity of each galaxy in Figure 8. The data points have large error bars associated with the photometry so that trends are difficult to determine. We see that the values for the LSBGs are consistent with those found for normal galaxies by Engelbracht et al. (2005), occupying similar parameter space as their high surface brightness counterparts in both plots. Most of our sample have relatively high 8 -to- $24\ \mu\text{m}$ flux ratios, so that the correlation of increasing R_2 with decreasing R_1 is not sampled by our galaxies. In fact, all the galaxies in our sample that are detected at both 8 and $24\ \mu\text{m}$ have R_2 larger than 0.2 , and all of the galaxies in the Engelbracht et al. (2005) with R_2 greater than this value have detected aromatic features. We see the same general metallicity trend as Engelbracht et al. (2005), with lower metallicity galaxies displaying weak aromatic emission, that is, diminishing $8\ \mu\text{m}$ flux density relative to $24\ \mu\text{m}$ flux density. One explanation for this trend is that harsh radiation fields in low-metallicity galaxies destroy PAH molecules (Galliano et al. 2003, 2005; Madden et al. 2006). This is unlikely to be the case for LSBGs, where the radiation fields are presumably not strong enough to destroy aromatics. Another explanation is that there are not enough carbon-rich asymptotic red-giant branch stars necessary to create large amounts of aromatic molecules in low-metallicity galaxies.

5. SUMMARY

Spitzer data on five low surface brightness galaxies indicate that a fraction of these objects contains modest amounts of dust, despite their low metallicities and apparent transparency. The LSBGs are detected at all IRAC wavelengths, and two are detected at all of the MIPS wavelengths. Those LSBGs and late-type high surface brightness counterparts that have detectable dust appear to be the same galaxies that have the largest amounts of star formation, while those that do not have detectable dust are the most diffuse, least star-forming galaxies (e.g., Malin 1). One explanation for this is that any dust existing in galaxies has to be heated to temperatures in the range 15 - $20\ \text{K}$ by ultraviolet photons escaping from star-forming regions before being detectable at far-IR and submillimeter wavelengths. The gathering evidence shows that modest amounts of dust can be created and maintained in a variety of environments and in galaxies of widely varying apparent formation histories. We also find that LSBGs exhibit less far-IR emission and greater variety in far-IR properties than is predicted by scaling related but higher surface brightness galaxy SEDs.

We thank Dean Hines and Jeroen Bouwman for allowing us to use the FEPS data reduction pipeline. This work is based on observations made with the *Spitzer* Space Telescope, which is operated by the Jet Propulsion Laboratory, California Institute of Technology under a contract with NASA. Support for this work was provided by NASA through an award issued by JPL/Caltech. This research has made use of the NASA/IPAC Extragalactic

² Available at <http://cas.sdss.org/dr5/en/>.

Database (NED) which is operated by the Jet Propulsion Laboratory, California Institute of Technology, un-

der contract with the National Aeronautics and Space Administration.

REFERENCES

- Barth, A. 2007, accepted to ApJ, astro-ph/0701018
- Bell, E. F., Barnaby, D., Bower, R. G., de Jong, R. S., Harper, D. A., Hereld, M., Loewenstein, R. F., & Rauscher, B. J. 2000, MNRAS, 312, 470
- Bendo, G. J., et al. 2003, AJ, 125, 2361
- Bothun G. D., Impey, C. D., Malin, D. F., & Mould, J. R. 1987, AJ, 94, 23
- Böttner, C., Klein, U., & Heithausen, A. 2003, A&A, 408, 493
- Braine, J., Herpin, F., & Radford, S. J. E. 2000, A&A, 358, 494
- Calzetti, D., et al. 2005, ApJ, 633, 871
- de Naray R. K., McGaugh, S. S., & de Blok, W. J. G. 2004, MNRAS, 355, 887
- Engelbracht, C. W., Gordon, K. D., Rieke, G. H., Werner, M. W., Dale, D. A., & Latter, W. B. 2005, ApJ, 628, L29
- Engelbracht, C. W., et al. 2007, accepted to PASP
- Fazio, G. G., et al. 2004, ApJS, 154, 10
- Galliano, F., Madden, S. C., Jones, A. P., Wilson, D. D., & Le Peintre, F. 2003, A&A, 407, 159
- Galliano, F., Madden, S. C., Jones, A. P., Wilson, C. D., & Bernard, J.-P. 2005, A&A, 434, 867
- Giovanelli, R., & Haynes, M. P. 1989, AJ, 97, 633
- Gordon, K. D., et al. 2005, PASP, 117, 503
- Gordon, K. D., et al. 2007, submitted to PASP
- Hines, D. C., et al. 2006, ApJ, 638, 1070
- Hinz, J. L., Misselt, K., Rieke, M. J., Rieke, G. H., Smith, P. S., Blaylock, M., & Gordon, K. D. 2006, ApJ, 651, 874
- Holwerda, B. W., Gonzalez, R. A., Allen, R. J., & van der Kruit, P. C. 2005, AJ, 129, 1396
- Houck, J. R., et al. 2004, ApJS, 154, 18
- Hunter, D. A., Elmegreen, B. G., & Martin, E. 2006, AJ, 132, 801
- Impey, C., & Bothun, G. 1989, ApJ, 341, 89
- Impey, C. D., Sprayberry, D., Irwin, M. J., & Bothun, G. D. 1996, ApJS, 105, 209
- Kessler, M. F., et al. 1996, A&A, 315, L27
- Knezek, P. M. 1993, Ph.D. Thesis
- Lagache, G., Abergel, A., Boulanger, F., & Puget, J.-L. 1998, A&A, 333, 709
- Lisenfeld, U., Israel, F. P., Stil, J. M., & Siever, A. 2002, A&A, 382, 860
- Madden, S. C., Galliano, F., Jones, A. P., & Sauvage, M. 2006, A&A, 446, 877
- Martin, D. C., et al. 2005, ApJ, 619, L1
- Matthews L. D., van Driel, W., & Monnier-Ragaigne, D. 2001, A&A, 365, 1
- McGaugh, S. S. 1992, Ph.D. Thesis
- McGaugh, S. S. 1994, ApJ, 426, 135
- McGaugh, S. S. & Bothun, G. D. 1994, AJ, 107, 530
- McGaugh, S. S., Schombert, J. M., & Bothun, G. D. 1995, AJ, 109, 2019
- Neugebauer, G., et al. 1984, ApJ, 278, L1
- O'Neil, K., Bothun, G. D., Schombert, J., Cornell, M. E., & Impey, C. D. 1997a, AJ, 114, 2448
- O'Neil, K., Bothun, G. D., & Impey, C. D. 1997b, Bulletin of the American Astronomical Society, 29, 1398
- Patterson, R. J. & Thuan, T. X. 1996, ApJS, 107, 103
- Pickering, T. E., Impey, C. D., van Gorkom, J. H., & Bothun, G. D. 1997, AJ, 114, 1858
- Pickering, T. E. 1998, Ph.D. Thesis
- Pickering, T. E., & van der Hulst, J. M. 1999, Astronomische Gesellschaft Meeting Abstracts, 15, 2
- Popescu, C. C., Tuff, R. J., Völk, H. J., Pierini, D., & Madore, B. F. 2002, ApJ, 567, 221
- Reach, W. T., et al. 1995, ApJ, 451, 188
- Rieke, G. H., et al. 2004, ApJS, 154, 25
- Roenback, J., & Bergvall, N. 1995, A&A, 302, 353
- Salzer, J. J., Lee, J. C., Melbourne, J., Hinz, J. L., Alonso-Herrero, A., & Jangren, A. 2005, ApJ, 624, 661
- Sauty, S., et al. 2003, A&A, 411, 381
- Scoville, N., & Young, J. S. 1983, ApJ, 265, 148
- Smith, J. D. T., et al. 2004, ApJS, 154, 199
- Smith, J. D. T., et al. 2006, ApJ, accepted, astro-ph/0610913
- Sodroski, T. J., Odegard, N., Arendt, R. G., Dwek, E., Weiland, J. L., Hauser, M. G., & Kelsall, T. 1997, ApJ, 480, 173
- Sprayberry, D., Impey, C. D., Bothun, G. D., & Irwin, M. J. 1995, AJ, 109, 558
- Spoon, H. W. W. 2003, Ph.D. thesis, Rijksuniversiteit Groningen
- Stansberry, J., et al. 2007, submitted to ApJ
- Stevens, J. A., Amure, M., & Gear, W. K. 2005, MNRAS, 357, 361
- Tuffs, R. J. & Popescu, C. C. 2005, AIR Conf. Proc. 761: The Spectral Energy Distributions of Gas-Rich Galaxies, 761, 344
- Vallenari, A., Schmidtobreick, L., & Bomans, D. J. 2005, A&A, 435, 821
- van der Hulst, J. M., Skillman, E. D., Smith, T. R., Bothun, G. D., McGaugh, S. S., & de Blok, W. J. G. 1993, AJ, 106, 548
- van Zee, L., Haynes, M. P., & Giovanelli, R. 1995, AJ, 109, 990
- van Zee, L. 2000, AJ, 199, 2757
- Wegner, G., Salzer, J. J., Jangren, A., Gronwall, C., & Melbourne, J. 2003, AJ, 125, 2373

TABLE 1
GALAXY PROPERTIES AND IMAGING OBSERVATION DATES

Galaxy	Morph. Type	Distance (km s ⁻¹)	$\mu_{0,B}$ (mag arcsec ⁻²)	M_B	Date IRAC	Date MIPS
Malin 1	S	24750	25.50 ^a	-22.50	2004 Jun 9	2005 Jan 30
UGC 5675	Sm:	1102	23.70 ^b	-12.95	2004 Apr 26	2004 Jun 2
UGC 6151	Sm:	1331	23.51 ^c	-17.21	2004 May 18	2004 Jun 4
UGC 6614	(R)SA(r)a	6351	24.30 ^d	-20.00	2003 Dec 19	2004 Jun 4
UGC 9024	S	2323	24.71 ^e	-16.58	2004 Jan 20	2004 Jul 10
UGC 6879	SAB(r)d	2383	20.40 ^f	-18.20	2004 Jun 9	2004 Jun 4
UGC 10445	SBc	963	21.79 ^g	-17.53	2004 Mar 8	2004 Mar 21

^aBothun et al. (1987)

^bMcGaugh & Bothun (1994)

^cPatterson & Thuan (1996)

^dvan der Hulst et al. (1993)

^eMcGaugh et al. (1995)

^fImpey et al. (1996)

^gvan Zee (2000)

TABLE 2
IRS OBSERVATION DETAILS

Galaxy	Date	IRS Mode	Integration Time (s)	P.A. (deg)
Malin 1	2005 Jan 4	SL	1707	-160.92
		LL	377.5	115.55
UGC 6879	2004 Jun 27	SL	1707	19.01
		LL	377.5	-64.50
UGC 10445	2004 Jul 14	SL	1707	42.37
		LL	377.5	-41.15

NOTE. — Complete details of observations can be retrieved via the SSC's Leopard database software.

TABLE 3
MIPS LSBG MORPHOLOGIES AND FLUX DENSITIES

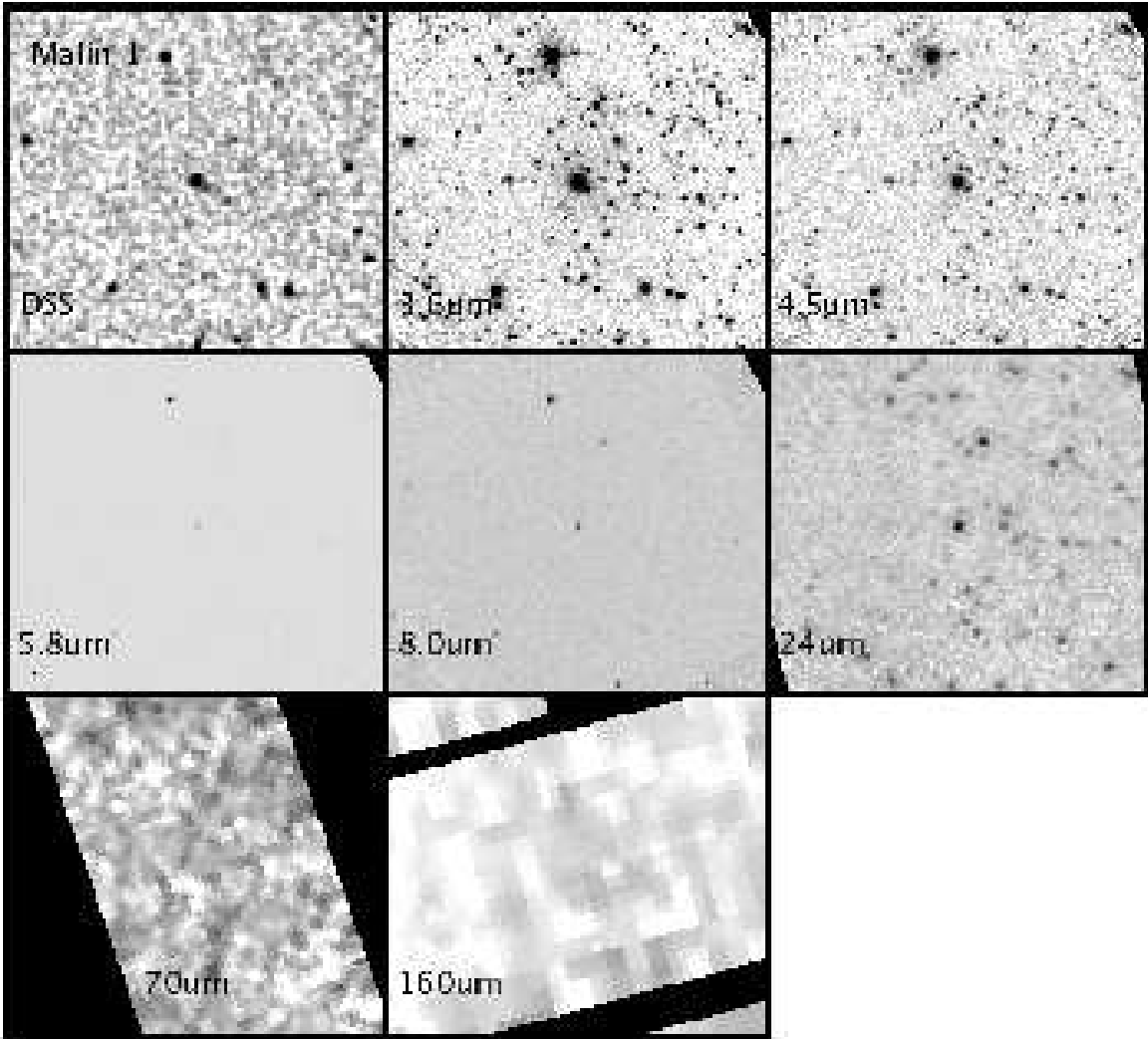
Galaxy	Morph. 24 μ m	Morph. 70 μ m	Morph. 160 μ m	F_ν (Jy) 24 μ m	Radius (")	F_ν (Jy) 70 μ m	Radius (")	F_ν (Jy) 160 μ m	Radius (")
Malin 1	point-like	no detection	no detection	4.3E-4±4.3E-5	24.90	< 0.004	...	< 0.01	...
UGC 5675	...	no detection	no detection	< 0.009	...	< 0.02	...
UGC 6151	extended	extended	extended	0.005 ± 5.0E-4	62.25	0.08 ± 0.02	49.25	0.29 ± 0.06	80
UGC 6614	extended	extended	extended	0.018 ± 2.0E-3	62.25	0.08 ± 0.02	54.18	0.38 ± 0.08	56
UGC 9024	point-like	point-like	no detection	0.001 ± 1.0E-4	24.90	0.04 ± 0.01	24.63	< 0.02	...
UGC 6879	extended	extended	extended	0.027 ± 3.0E-3	62.25	0.44 ± 0.09	54.18	1.47 ± 0.29	56
UGC 10445	extended	extended	extended	0.025 ± 2.0E-3	105.8	0.55 ± 0.11	98.50	2.50 ± 0.50	120

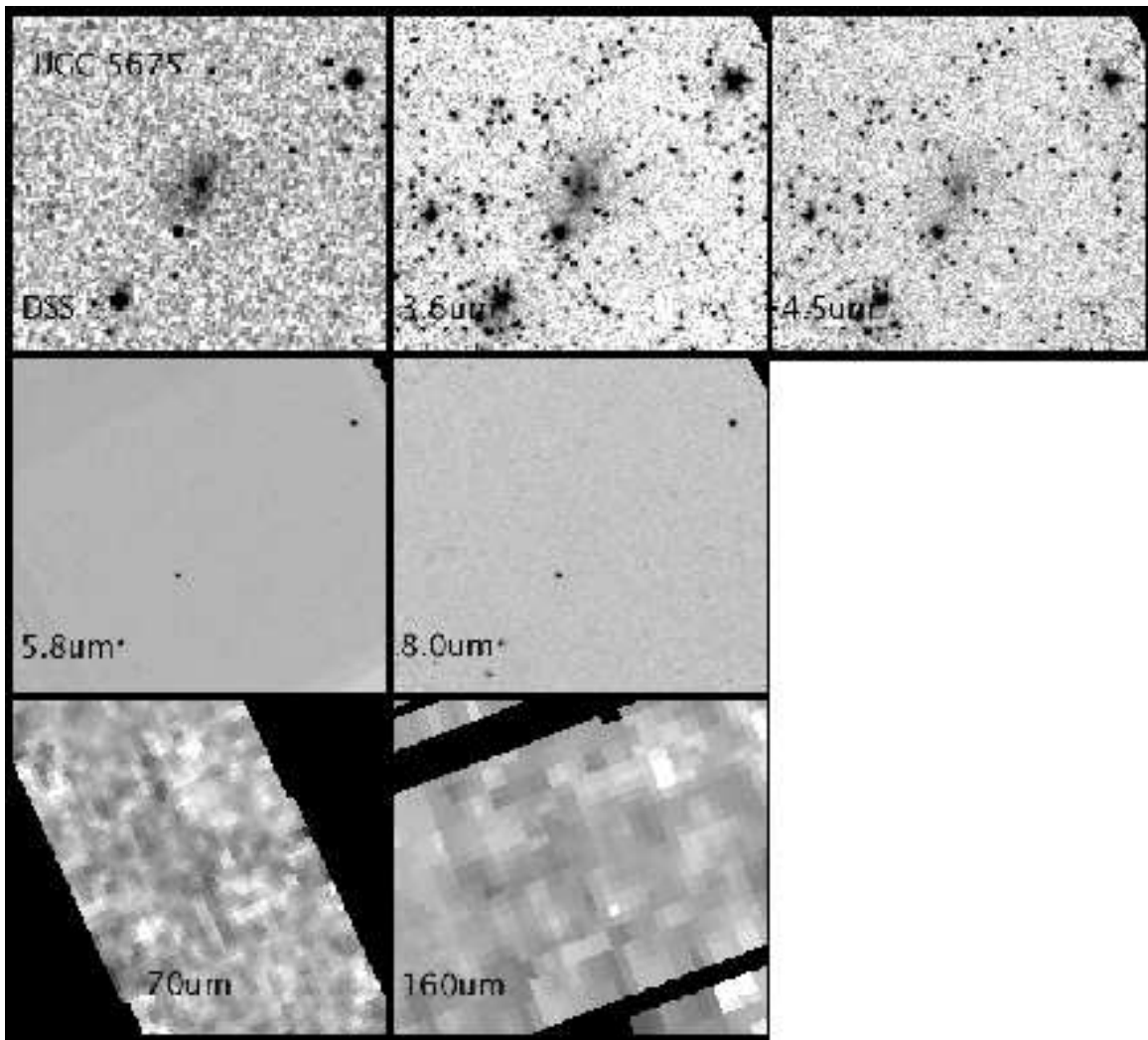
TABLE 4
IRAC FLUX DENSITIES

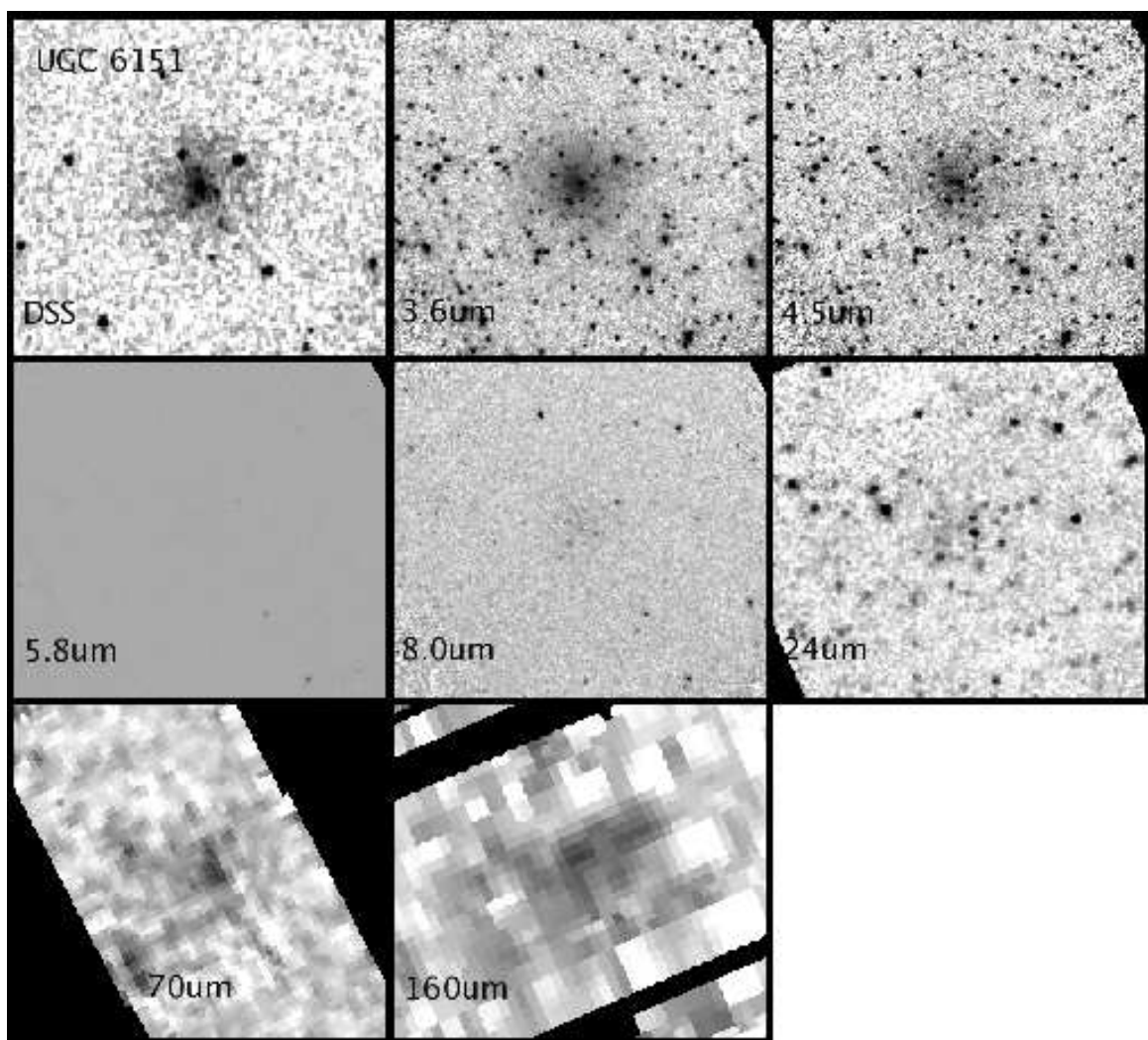
Galaxy	F_ν (Jy) 3.6 μ m	F_ν (Jy) 4.5 μ m	Radius (")	F_ν (Jy) 5.8 μ m	F_ν (Jy) 8.0 μ m	Radius (")
Malin 1	1.74E-3±1.74E-4	1.20E-3±1.20E-4	18	6.87E-4±1.03E-4	1.03E-3±1.55E-4	18
UGC 5675	1.22E-3±1.22E-4	7.47E-4±7.47E-5	30	< 2.03E-5	< 1.18E-4	...
UGC 6151	4.60E-3±4.60E-4	2.87E-3±2.87E-4	60	2.47E-3±3.71E-4	4.15E-3±6.23E-4	60
UGC 6614	2.45E-2±2.45E-3	1.43E-2±1.43E-3	108	1.66E-2±2.49E-3	2.43E-2±3.65E-3	60
UGC 9024	3.10E-3±3.10E-4	2.00E-3±2.00E-4	60	9.00E-4±1.35E-4	2.00E-3±3.00E-4	24
UGC 6879	2.15E-2±2.15E-3	1.39E-2±1.39E-3	108	2.05E-2±3.08E-3	4.71E-2±7.07E-3	60
UGC 10445	2.00E-2±2.00E-3	1.60E-2±1.60E-3	78	2.10E-2±3.15E-3	3.40E-2±5.10E-3	78

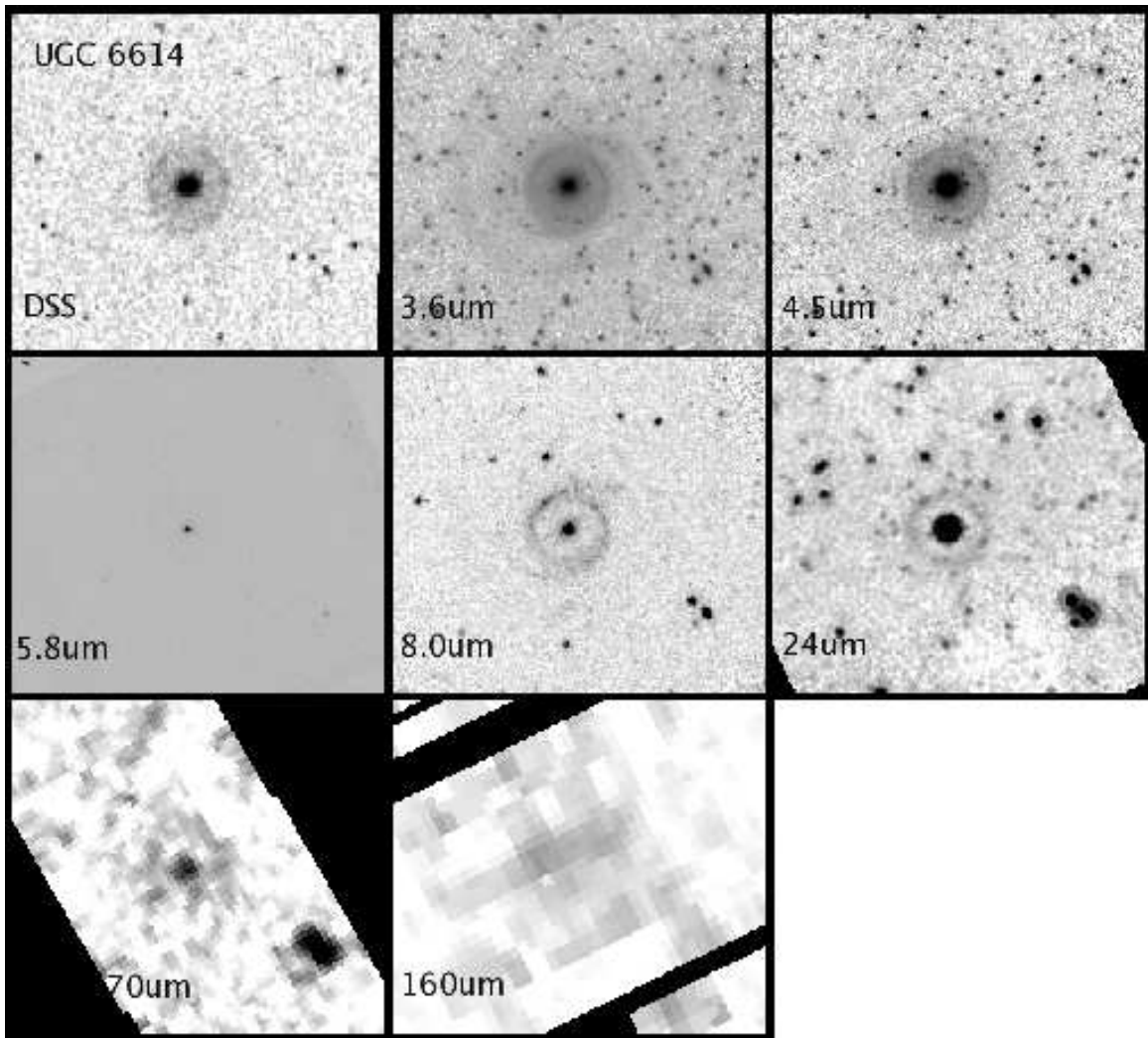
TABLE 5
IRS FLUXES OR EWs FROM PAHFIT

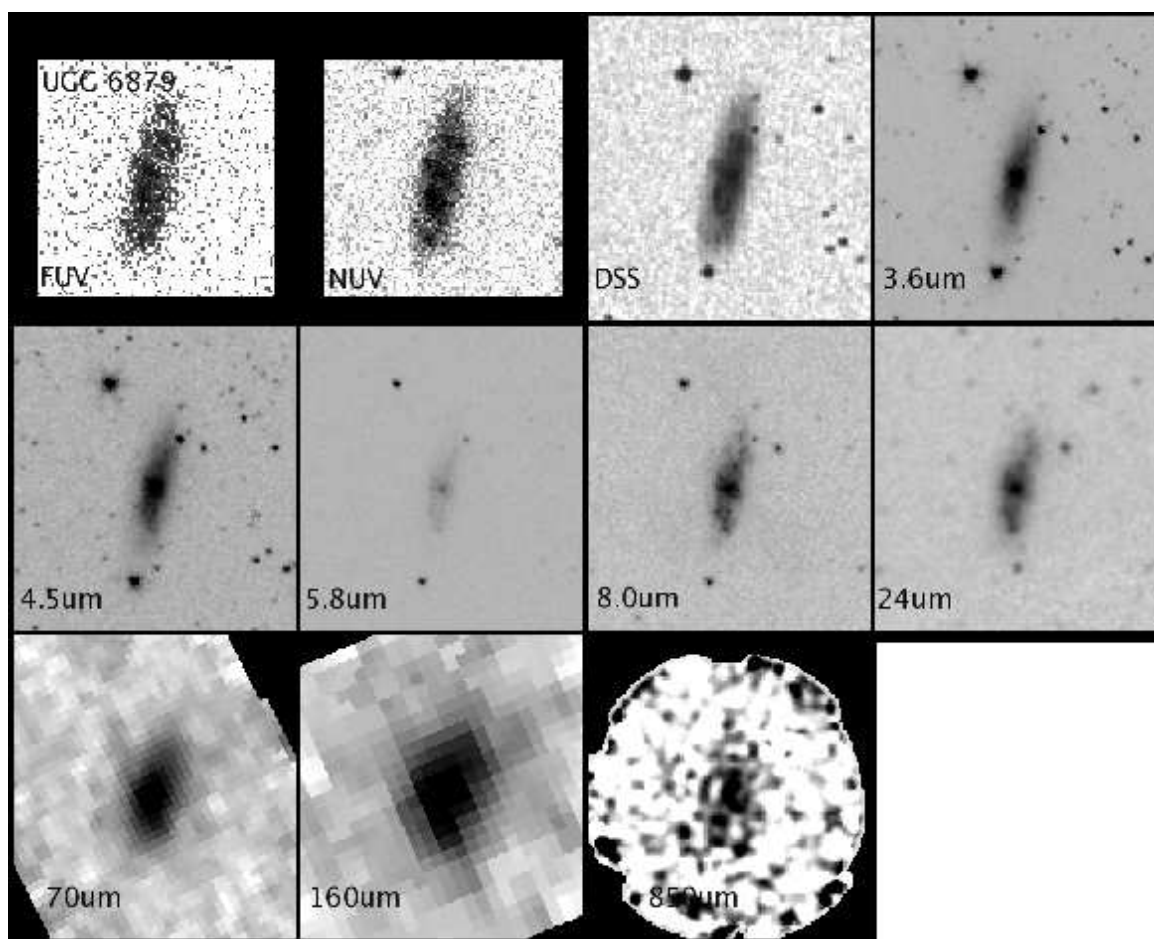
Feature	Flux (erg s ⁻¹ cm ⁻²)
UGC 6879	
[S IV]	4.89E-16±3.86E-16
[Ne II]	4.98E-15±4.74E-16
[S III]	7.14E-15±1.45E-15
7.7 μm complex EW	13.57±0.68 μm
UGC 10445	
[S IV]	2.36E-15±3.75E-16
[Ne II]	4.20E-15±4.30E-16
[S III]	2.39E-15±1.63E-15
7.7 μm complex EW	5.69±1.83 μm











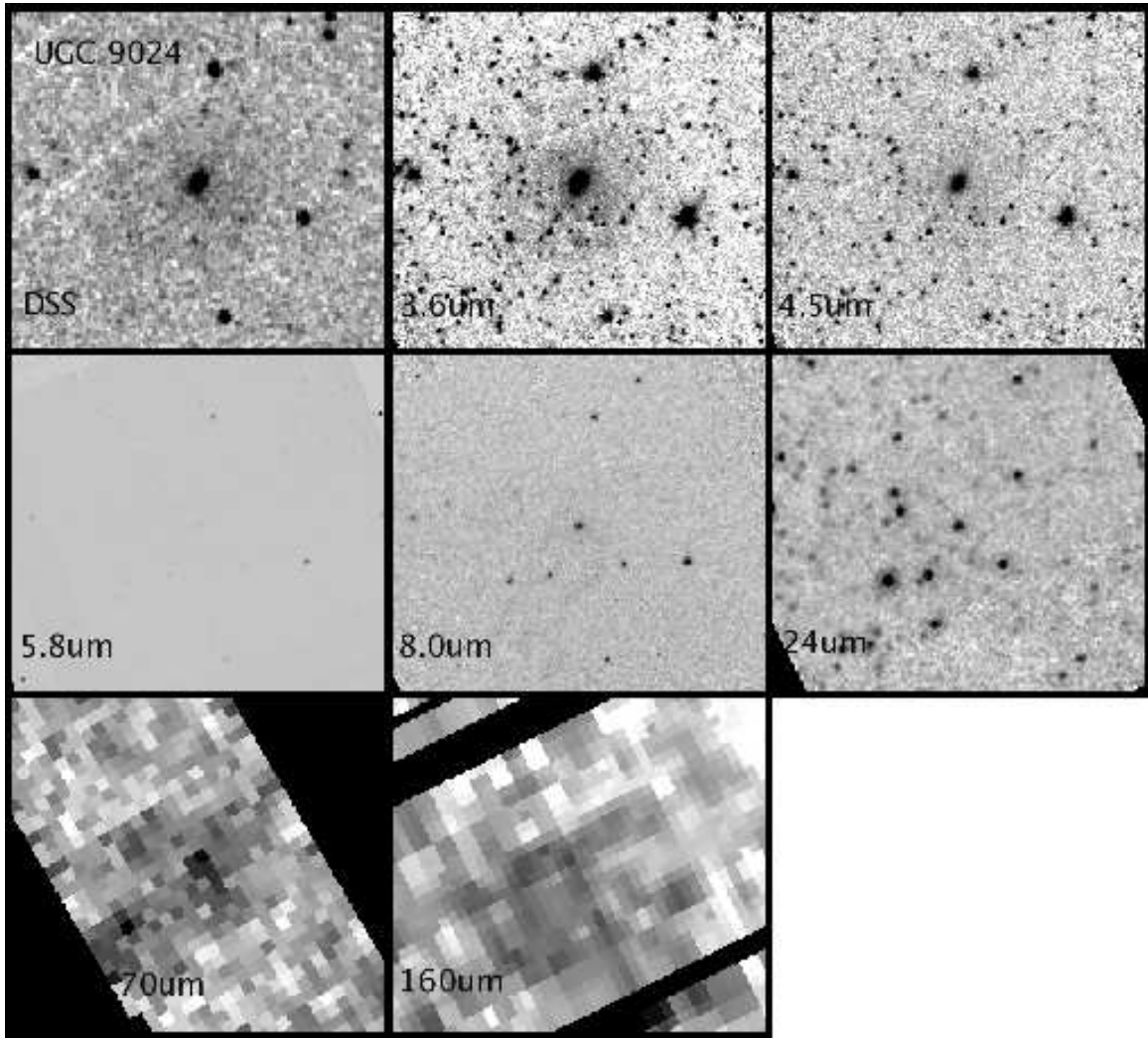


FIG. 1.— Multi-wavelength views of the galaxy sample. North is up and east is to the left. The field of view of each panel is $\sim 4'.5 \times 4'.5$. The panels, from right to left, starting on the top row: Digitized Sky Survey (DSS), the four IRAC bands, the three MIPS bands. The exception to this is UGC 6879 which has: *GALEX* far-UV, *GALEX* near-UV, DSS, IRAC, MIPS, and SCUBA $850 \mu\text{m}$. The scale for the DSS image is $1''.7$ and for *GALEX* it is $5''$. Pixel scales for all IRAC images are $1''.2$. Pixel scales for the MIPS images are $1''.245$ for $24 \mu\text{m}$, $4''.925$ for $70 \mu\text{m}$, and $8''.0$ for $160 \mu\text{m}$. The SCUBA image has been rebinned to $1''$ pixels from an original beamwidth of $15''$.

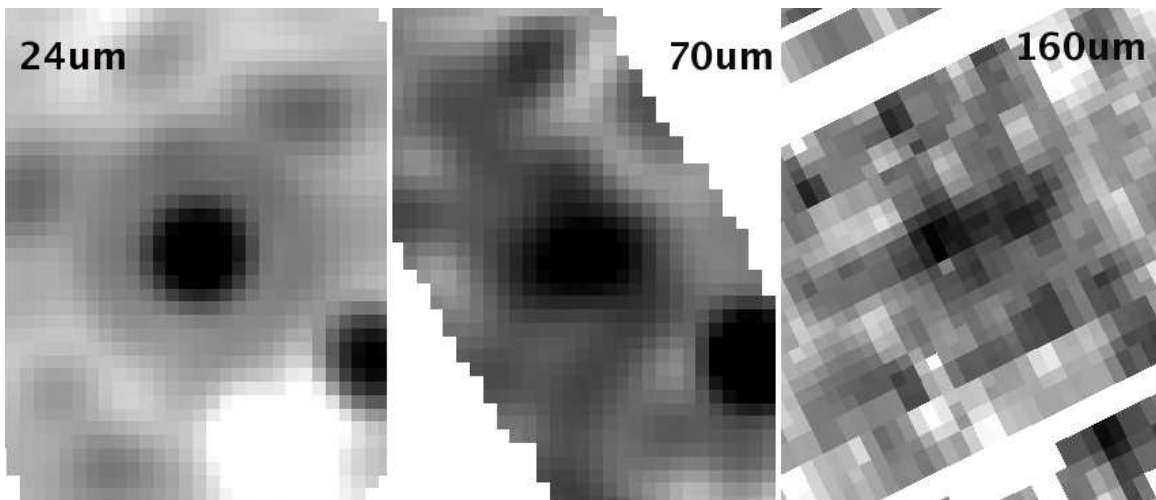


FIG. 2.— UGC 6614 at 24 , 70 , and $160 \mu\text{m}$. The 24 and $70 \mu\text{m}$ images are convolved to the $160 \mu\text{m}$ resolution. The changing morphology and brightness of the galaxy at far-IR wavelengths does not appear to be a result of the resolution differences. North is up and east is to the left. The field of view of each panel is $\sim 4'.0 \times 4'.8$.

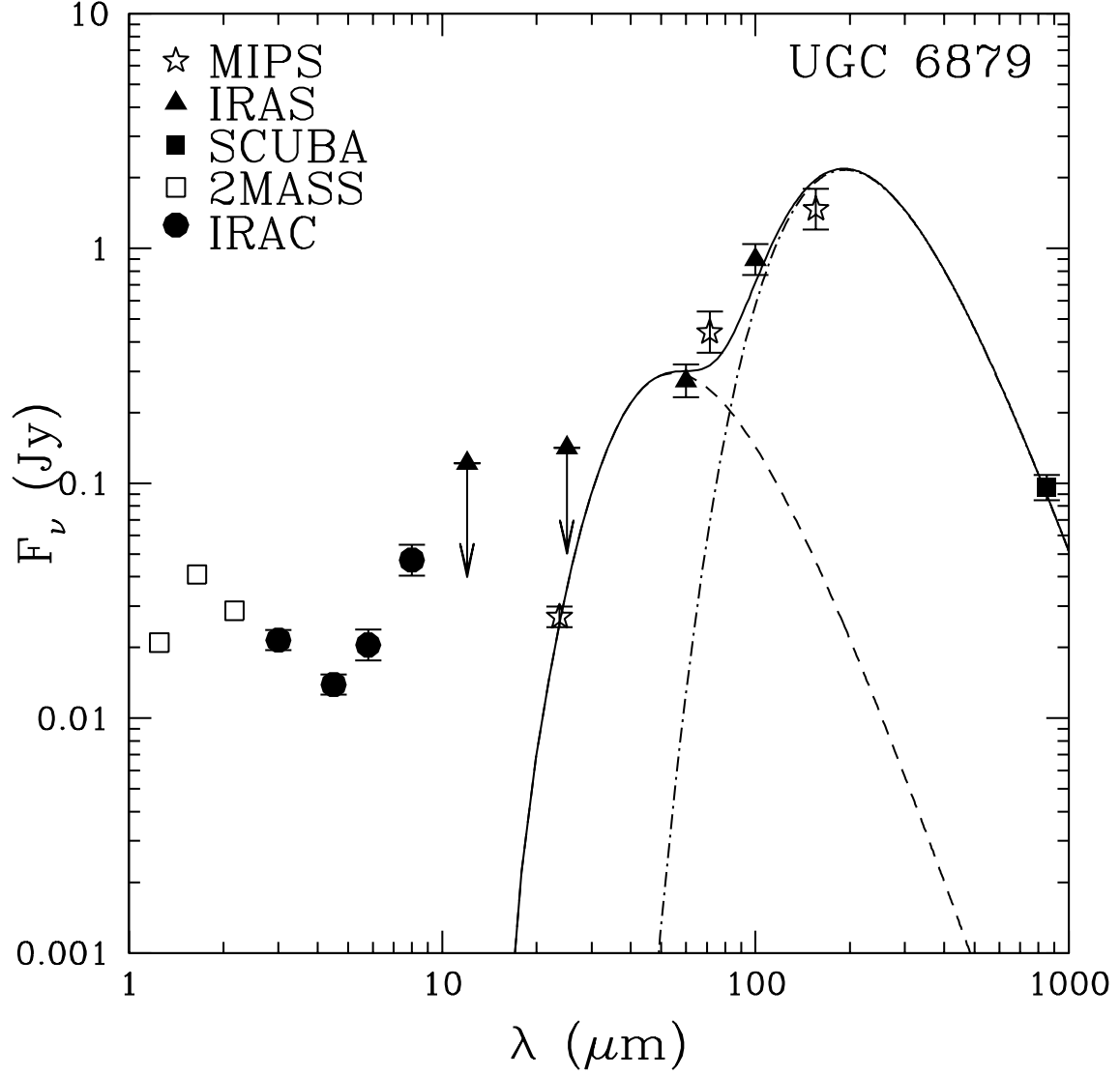


FIG. 3.— Spectral energy distribution of UGC 6879 showing *GALEX*, 2MASS, IRAC, *IRAS*, MIPS, and SCUBA data points. The *IRAS* data points at 12 and $25\ \mu\text{m}$ are upper limits only. The solid line is a two-component dust model fitted to the four IRAC data points, two *IRAS* points, and three MIPS points. This model consists of a warm silicate component at $T = 52\text{ K}$ (*dashed line*) and a cool silicate component at $T = 15\text{ K}$ (*dashed-dotted line*).

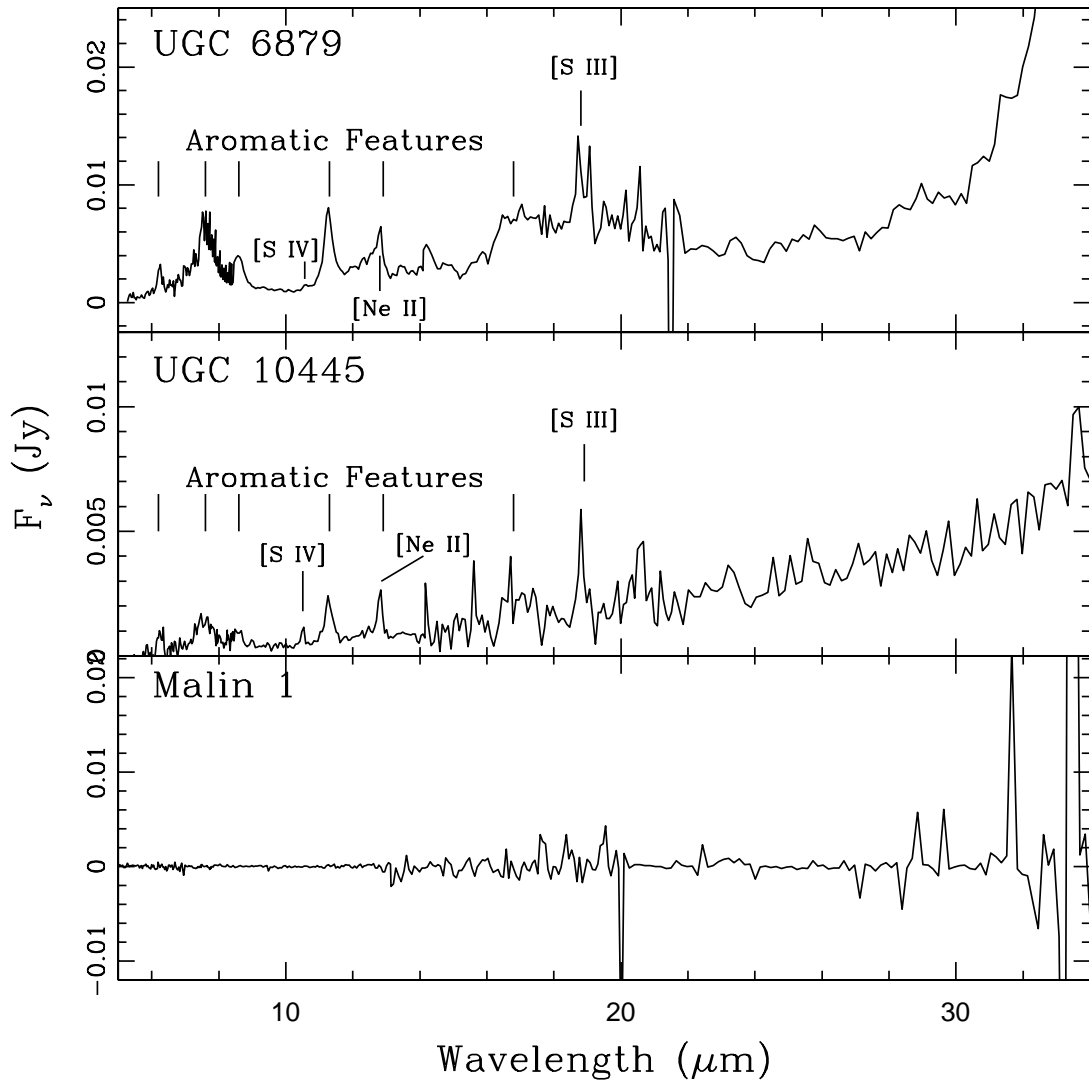


FIG. 4.— IRS spectra, rest wavelength versus flux density, for UGC 6879, UGC 10445, and Malin 1. The broad aromatic features and emission lines are indicated on the top and middle panels on both the UGC 6879 and UGC 10445 spectra. The Malin 1 spectrum is consistent with noise.

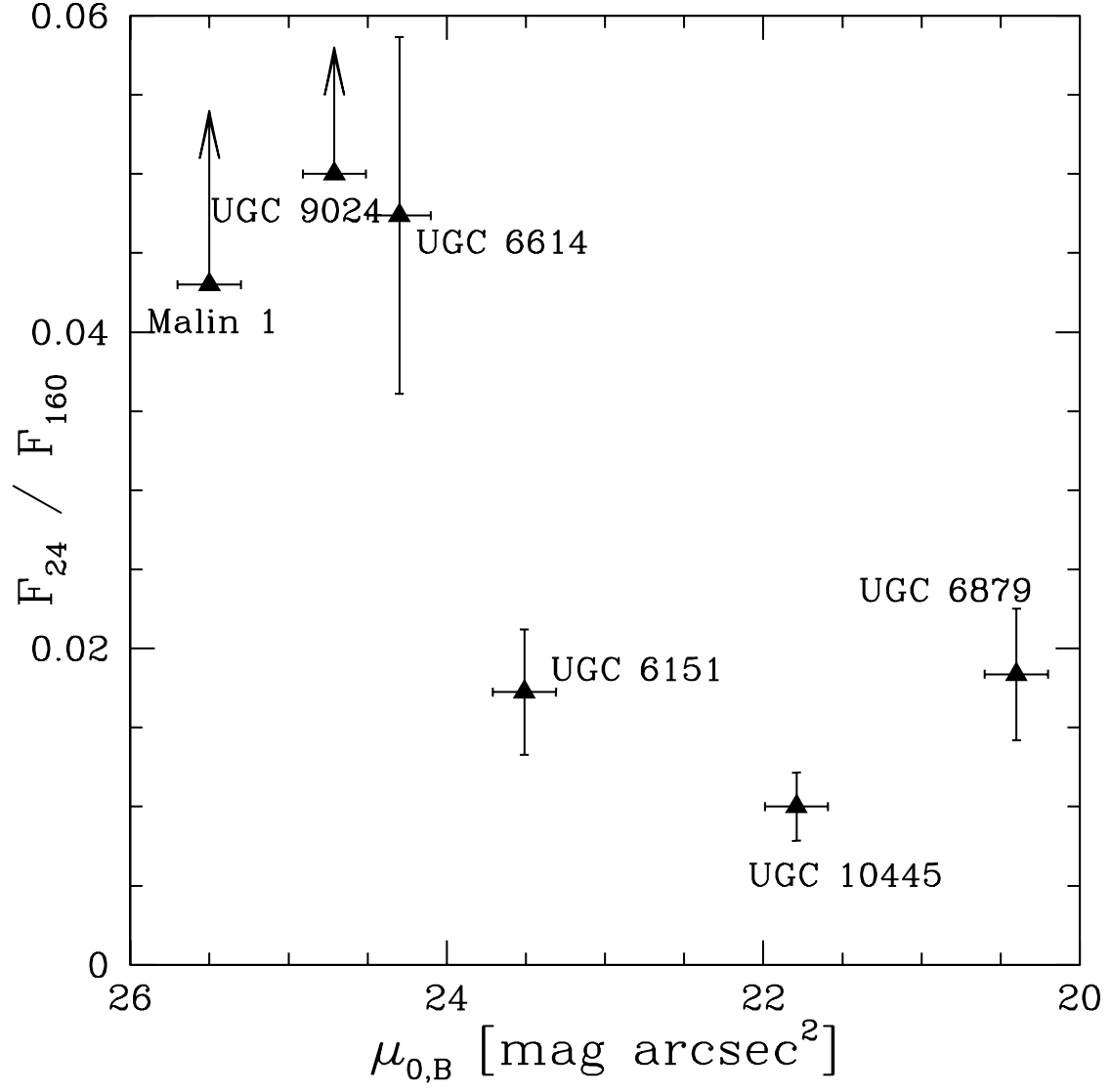


FIG. 5.— B -band central surface brightnesses of the galaxy sample versus the ratio of the flux densities at 24 and 160 μm . All objects are included except UGC 5675, which does not have data at 24 μm . Lower limits are given for Malin 1 and UGC 9024, which are not detected at 160 μm .

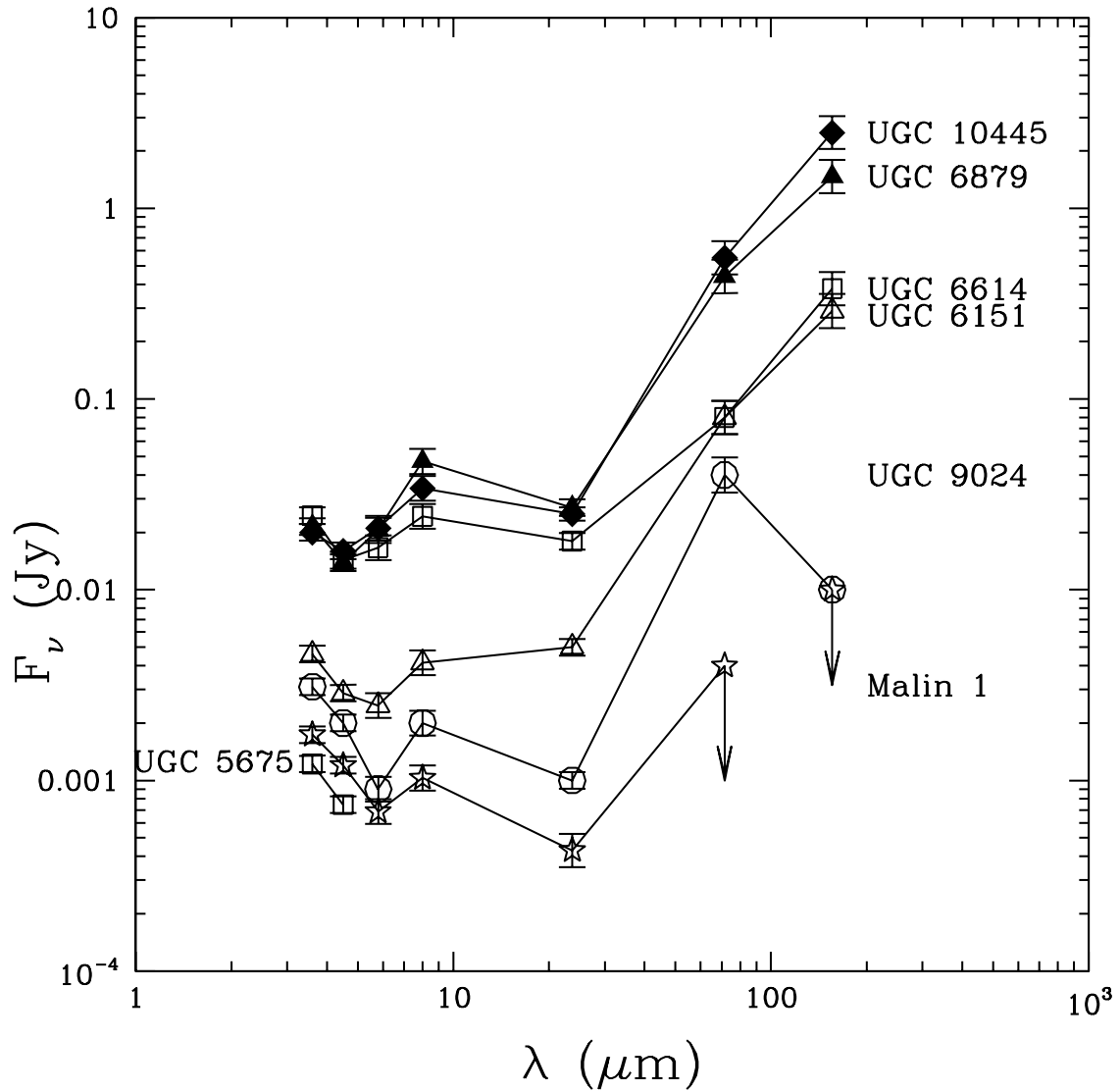


FIG. 6.— Spectral energy distributions of all the galaxies showing the IRAC and MIPS data points. The high surface brightness galaxy data are shown in solid points while the LSBG data are shown in open points. The arrows represent 3σ upper limits at 70 and 160 μm .

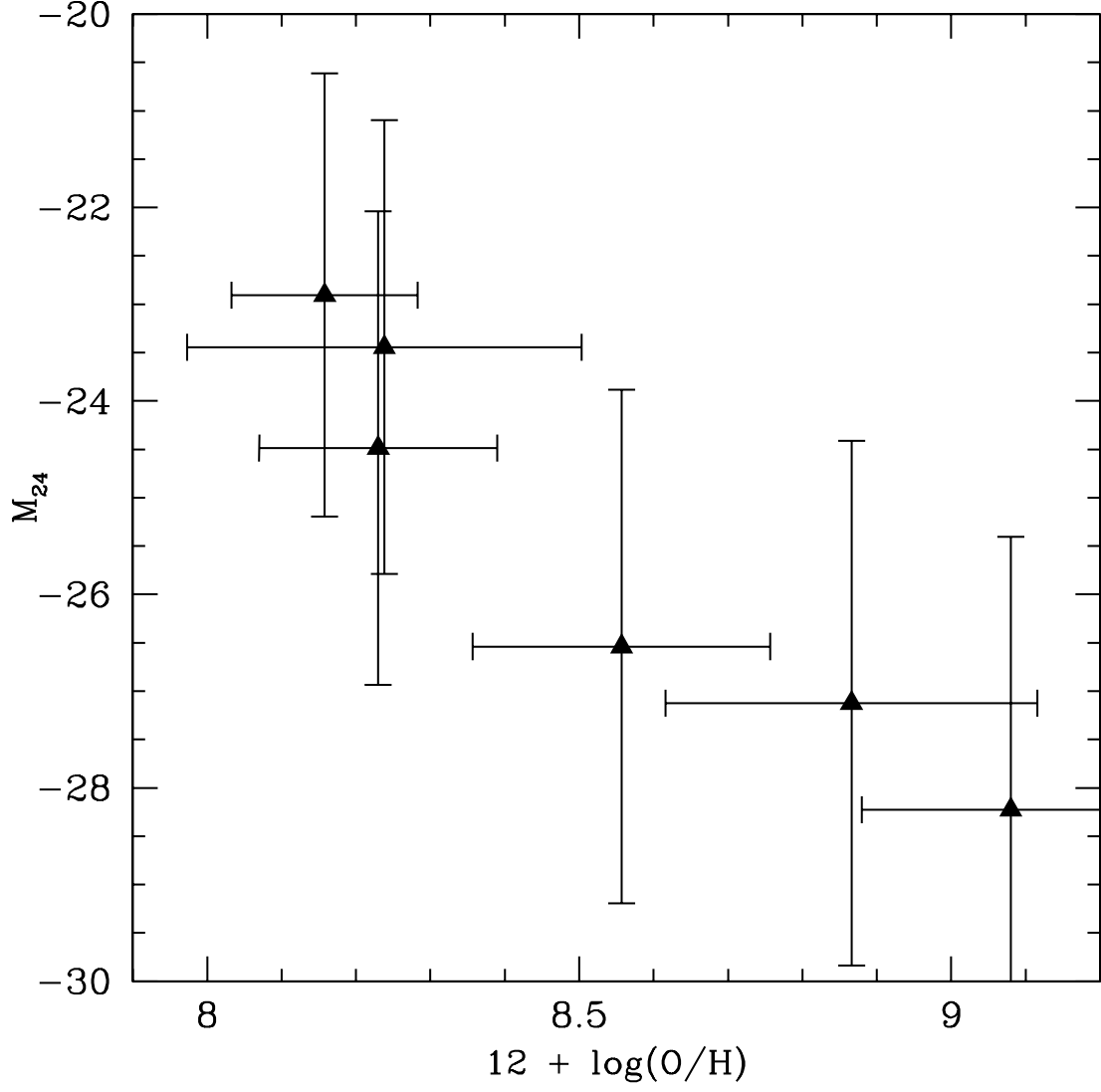


FIG. 7.— Metallicity and absolute magnitude at $24\mu\text{m}$ for all the galaxies except UGC 5675, where $24\mu\text{m}$ data are not available. While it would be expected for the galaxies to follow the $L - Z$ trend, the difficulty in determining metallicities seems to have weakened the correlation.

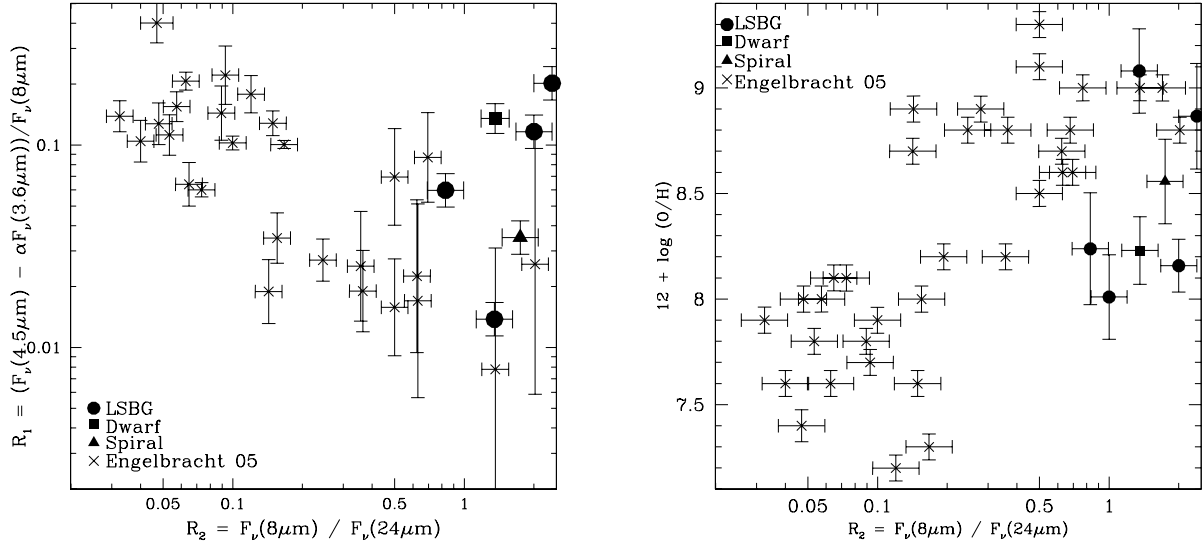


FIG. 8.— On the left, mid-infrared colors of the galaxy sample, with R_1 and R_2 defined as in Engelbracht et al. (2005), and, on the right, galaxy metallicity as a function of the 8-to-24 μm color, R_2 . Solid circles represent LSBGs, the solid square represents UGC 10445, and the solid triangle represents UGC 6879. The data points from Engelbracht et al. (2005) are shown as crosses. There is a slight upward trend of increasing aromatic strength with increasing metallicity.